Commun. Comput. Phys.
doi: 10.4208/cicp.2009.09.069

Vol. **8**, No. 1, pp. 95-114
July 2010

A Model Study on the Generation of Internal Tides by Tidal Flows Over a Submerged Seamount in the Channel

Shuqun Cai[1,*], Junliang Liu[1,2] and Xiaomin Long[1]

[1] *LED, South China Sea Institute of Oceanology, Chinese Academy of Sciences, Guangzhou, 510301, China.*
[2] *Graduate School of the Chinese Academy of Sciences, Beijing, 100049, China.*

Received 22 April 2009; Accepted (in revised version) 22 October 2009

Communicated by Lianjie Huang

Available online 12 February 2010

Abstract. It is known that the submerged seamount/ridge is a source for the generation of internal tides. In this paper, a three-dimensional two-layer model is set up to study the generation of internal tides by tidal flows over a submerged seamount/ridge in the channel. Several numerical experiments with different topographic features, upper layer depths, tidal flows and background currents are carried out to study the variations of the induced internal tides. It is shown that, for the specific stratification, the seamount feature, the slope, the initial upper layer depth and the imposing driven force determine the Froude number near the seamount peak. Once when the Froude number is supercritical, the associated maximum amplitude of the induced internal tide is so large that the internal tide begins to disintegrate, which brings about severe variations of the current velocity and the water elevation fields, and the associated induced baroclinic tidal energy around the seamount peak is much larger than the barotropic one. The Richardson number greater than 1/4 is a criterion for stability of shear flow. Since the maximum tidal velocity changes within $0 \sim 360^\circ$ with time in a period around the seamount peak, the induced internal tide does not stride the seamount peak before it disintegrates, which is different from the two-dimensional modeled results. The asymmetrical slope of the submerged seamount is a mechanism for the asymmetrical internal tide generation.

AMS subject classifications: 76B55, 76E20, 76M20

Key words: Internal tides, numerical modeling, two-layer model, sill channel.

*Corresponding author. *Email addresses:* caisq@scsio.ac.cn (S. Cai), lerry710@scsio.ac.cn (J. Liu), xmlong@scsio.ac.cn (X. Long)

1 Introduction

The sill straits among the Luzon Strait are the sources for the generation of internal solitary waves (Fig. 1, literature [1,2]). It is interesting that almost all internal solitary waves are observed to propagate westward to the northern South China Sea (SCS), whilst few are observed to propagate eastward to the Pacific [3]. Zheng et al. [4] suggested that the eastward propagating disturbances have no chance to grow up into internal solitary waves, so that they hardly appear on the east side of the submarine ridges in the eastern Luzon Strait. According to the numerical results based on a two-dimensional (i.e., in the directions of x and z) composite model in the Luzon Strait [2], it is shown that only when the amplitude of an internal tide is large enough would a train of internal solitary waves be induced, and a constant mean westward background flow in the Luzon Strait has a great damping effect on the amplitude of the induced internal tide toward the Pacific, thus the induced internal tide toward the Pacific has no chance to grow up into internal solitary waves. However, some questions about this asymmetrical propagation of the internal solitons in the Luzon Strait remain unknown, e.g., according to the previous studies [5,6], the background current in the Luzon Strait is not always westward, which may not support the conclusion by Cai et al. [2] that the westward propagation of the induced internal solitons is due to the westward background current. Therefore, is there any other key factor affecting the asymmetrical propagation of the internal solitons in the northern SCS?

Usually the problem on the generation and propagation of internal solitary waves is separated into a "generation phase", for which the hydrostatic approximation is applied [7,8], and a "propagation phase", for which a nonhydrostatic description is required [9, 10]. To simplify the question, we limit our study to the generation of internal tides, since Cai et al. [2] showed that only when the amplitude of the induced internal tide is large enough could a train of internal solitary waves be released and propagate away from the source. Thus, if we could reveal some characteristics of the asymmetrical distribution of the internal tide generation, we may find the key factor affecting the asymmetrical propagation of internal solitons.

The submerged seamount or ridge is a source for the generation of internal tides, e.g., Dushaw et al. [11] found that the significant semidiurnal internal tide in the deep ocean far away from the north of Hawaiian Islands is generated over the Hawaiian Ridge, and it is testified by the three-dimensional POM model study [12]. Numerical modeling around Fieberling Guyot in response to tidal flows [13,14] had been carried out before. Recently, there are some three-dimensional continuously stratified layers models studies on the internal waves generation by different bottom topographies [15–18]. However, the horizontal distributions of the induced barotropic and baroclinic tidal energies by submerged seamounts or ridges, especially in a sill channel, have still not been clearly revealed by them.

In this paper, we try to study the above problem based on a three-dimensional two-layer model forced by barotropic tidal flows. We limit our simulation domain to the

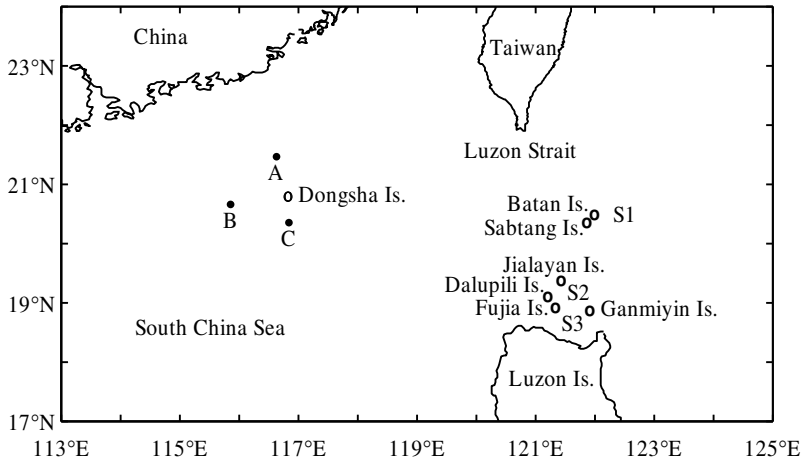

Figure 1: Sketch of the observational sites (A, B and C) and possible source sites (S1, S2 and S3) of the internal solitons in the South China Sea (S1 denotes the channel between the Batan and Sabtang islands, S2 between the Jialayan and Dalupili islands, while S3 between the Fujia and Luzon islands).

small-scale sill channel, similar to that between the Batan and Sabtang islands in the Luzon Strait [2]. In the following, the model description and choice of parameters are given in Section 2. In Section 3, the numerical experimental results and discussions are presented, and Section 4 is the conclusion.

2 Description and choices of parameters of the two-layer model

In reality, the ocean is continuously stratified, however, the simplification of two superposed fluids of different density that are immiscible (e.g., the well mixed layer water and the water below in the ocean) is considered for the mechanism study of internal waves by many authors [10, 19], since the major first baroclinic mode of internal wave could be revealed by a two-layer model. The model set up here is a three-dimensional two-layer hydrostatic approximation model based on the two-dimensional one [2]. The means of describing the situation is shown in Fig. 2a, where the subscripts 1 and 2 refer to the upper and lower layer, respectively. The free sea surface displacement, whose equilibrium position is $Z=0$, has perturbed position $Z=\eta_1$, the interface displacement is η_2 (it is also called as the pycnocline height anomaly, or PHA in short), $h_1=H_1+\eta_1-\eta_2$, $h_2=H_2+\eta_2$, H_1 and H_2 are the undisturbed initial depths within the upper and lower layers, and the initial water depth $H=H_1+H_2$. The free surface boundary conditions are given by the kinematic condition,

$$W=0 \qquad \text{at } Z=\eta_1 \tag{2.1}$$

and the dynamic condition

$$p=0 \qquad \text{at } Z=\eta_1 \tag{2.2}$$

where W is the vertical velocity and p is pressure. At the interface, the kinematic condition is,

$$W=0 \qquad \text{at } Z=-h_1 \tag{2.3}$$

it follows from the hydrostatic equation $\frac{\partial p}{\partial Z}=-\rho g$ and the dynamic condition is that the pressure in both layers is equal, i.e.,

$$p=-\rho g h_1 \qquad \text{at } Z=-h_1 \tag{2.4}$$

and the bottom boundary condition is,

$$W=0 \qquad \text{at } z=-H. \tag{2.5}$$

Retaining only the first term in the perturbation expansion for the advective terms, the vertically integrated equations of motion used in the models are [19,20],

$$\begin{aligned}
&\frac{\partial \overrightarrow{V_1}}{\partial t}+(\nabla\cdot\overrightarrow{V_1}+\overrightarrow{V_1}\cdot\nabla)\overrightarrow{v_1}+\overrightarrow{k}\times f\overrightarrow{V_1}\\
&\quad=-(H_1+\eta_1-\eta_2)g\nabla\eta_1-\overrightarrow{\tau_I}/\rho_1+A_H\nabla^2\overrightarrow{V_1}, &(2.6)\\
&\frac{\partial \overrightarrow{V_2}}{\partial t}+(\nabla\cdot\overrightarrow{V_2}+\overrightarrow{V_2}\cdot\nabla)\overrightarrow{v_2}+\overrightarrow{k}\times f\overrightarrow{V_2}\\
&\quad=-(H_2+\eta_2)[(g-g')\nabla\eta_1-g'\nabla(H_1-\eta_2)]+(\overrightarrow{\tau_I}-\overrightarrow{\tau_B})/\rho_2+A_H\nabla^2\overrightarrow{V_2}, &(2.7)\\
&\frac{\partial(\eta_1-\eta_2)}{\partial t}+\nabla\cdot\overrightarrow{V_1}=0, &(2.8)\\
&\frac{\partial\eta_2}{\partial t}+\nabla\cdot\overrightarrow{V_2}=0, &(2.9)\\
&\overrightarrow{\tau_I}=\rho_1 C_I\overrightarrow{(v_1-v_2)}\left|\overrightarrow{(v_1-v_2)}\right|, &(2.10)\\
&\overrightarrow{\tau_B}=\rho_2 C_B\overrightarrow{v_2}\left|\overrightarrow{v_2}\right|. &(2.11)
\end{aligned}$$

Here, ρ is the water density, $\overrightarrow{V_i}$ and $\overrightarrow{v_i}$ ($i=1,2$) are vertical integral transport and depth-mean velocity, respectively, $g'=g(\rho_2-\rho_1)/\rho_1=g\Delta\rho/\rho_1$ is reduced gravity acceleration. $\overrightarrow{\tau_I}$ and $\overrightarrow{\tau_B}$ denote interfacial and bottom friction stress, C_I and C_B are the coefficients of interface and bottom friction, respectively. The Coriolis parameter $f=2\Omega\sin\varphi$, Ω is the earth angular velocity and φ is the latitude (here we set $\varphi=20.4^\circ$N, where the latitude is near the channel between the Batan and Sabtang islands in Fig. 1), and A_H is the lateral friction coefficient.

The coefficient of bottom friction is changed with the bottom topography [21], i.e.,

$$C_B=\begin{cases} C_{B1}\times(300-H)/300, & H\leqslant 300\text{m},\\ 0, & H>300\text{m}, \end{cases} \tag{2.12}$$

where C_{B1} is the basic coefficient of bottom friction.

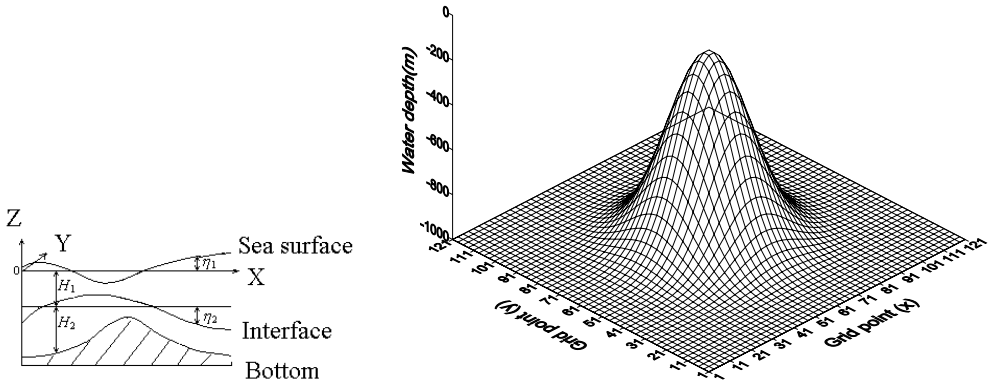

(a) (b)

Figure 2: (a) Sketch of the two-layer model, and (b) bottom topography in the channel (unit: m).

Many previous model studies have been limited to idealized Gaussian-shaped seamounts. Here, the bathymetry is also defined through a Gaussian distribution as [12],

$$h(x,y)=H-h_0\exp\left[-\frac{(x-x_0)^2}{a^2}-\frac{(y-y_0)^2}{b^2}\right], \tag{2.13}$$

where $H=1000$m is the maximum water depth, $h_0=840$m is the height of the topographic feature above the seabed, $h(x,y)$ is the water depth, and (x_0,y_0) is set at the center of the model domain. The values of a and b define the width of the feature. If $a=b$, the feature is referred to as a submerged seamount (Fig. 2b, the seamount is centered at the middle of the channel); if $a>b$ $(a<b)$, the feature becomes a ridge along the y (x) direction. The Gaussian-shaped topographies are defined with steep slopes. Both the north and south boundaries are solid walls, whilst the east and west boundaries are open.

The model is forced by the following barotropic tidal current in the upper layer at the east open boundary,

$$u_{1e}=A_0+A_1\cos\left(\frac{2\pi}{T}t\right). \tag{2.14}$$

Here, A_0 is the background current (usually $A_0=0$), A_1 is the tidal flow amplitude, T is the tidal period (here we set $T=12.42$h for M_2 tide), and t is the time. For the upper layer current at the west open boundary, and for the lower layer current at both east and west open boundaries, a radiation boundary condition [22],

$$\frac{\partial\phi}{\partial t}+C\frac{\partial\phi}{\partial x}=0 \tag{2.15}$$

is used, where ϕ is any variable stated above, and C is the phase velocity of the waves. According to several sensitive experiments, it is found that, within the 10 grids away from the both open boundaries, when a sponge boundary condition [23] is used, the energy

Table 1: Experimental cases with different conditions.

E1	Imposing tidal flow amplitude at east open boundary $A_1=8.0$cm/s, $A_0=0$, $H_1=80$m, and $a=b=1000$, with a symmetric slope of about 27.8°
E2	Same as E1, but $a=1000$ and $b=1200$
E3	Same as E1, but $a=b=2500$, with a symmetric slope of about 12.1°
E4	Same as E1, but $H_1=70$m
E5	Same as E1, but $H_1=85$m
E6	Same as E1, but the imposing tidal current amplitude at eastern boundary $A_1=8.8$cm/s
E7	Same as E1, but the imposing tidal flow amplitude at east open boundary $A_1=5.9$cm/s and $A_0=-0.5$cm/s
E8	Same as E1, but the slope is about 27.8° in the western half part of the channel whilst it is about 12.1∘ in the eastern half part

reflection at the open boundaries can be effectively prevented. In the solid boundaries of the channel, a no-slip condition is prescribed on the tangential flow.

In the computation, the above Eqs. (2.6)-(2.11) about η_i and $\overrightarrow{V_i}$ ($i=1$, 2) are solved on 'Arakawa C' grid using a similar semi-implicit scheme [20]. The time differencing is leapfrog, for advection a Scheme C from Grammeltvedt [24] is used, the Holland and Lin [25] scheme is used for the Coriolis force, and the horizontal friction is lagged in time for computational stability. Finally, by taking the divergence of momentum equations and substituting into the continuity equations, the problem is reduced to the solution of Helmholtz equations in favor of η_1/η_2 in case of the above prescribed boundary conditions for $\overrightarrow{V_i}$ ($i=1$, 2).

The coefficients of interface and bottom friction are $C_I=0$ and $C_{B1}=2\times10^{-3}$, respectively, and the lateral friction coefficient is $3\text{m}^2\text{s}^{-1}$. The relative density difference value between the upper and lower layer is $\Delta\rho/\rho=0.001$. The computational domain is within a square with a side of 6km, the gird size is 50m and the time step is 30s.

3 Simulation experiments results and discussions

Seven experiments are designed (Table. 1). Each experiment starts from the rest state and gets quasi-equilibrium after running about 1 tidal period, and the data from the 2$^{\text{nd}}$ to the 6$^{\text{th}}$ tidal period are saved for analyses. In the standard experiment E1, the seamount is symmetric with a steep slope of about 27.8°, and it is driven by the imposing tidal flow at the east boundary with $A_1=8.0$cm/s. The other experiments are designed to test whether the variations of the seamount feature, the slope, the initial upper layer depth and the imposing driven force affect the characteristics of the induced internal tides or not.

3.1 Experiment E1

To facilitate easy comparisons, before discussing the three-dimensional simulation results, we would like to simply describe the processes of the disintegrating of the internal tide and the propagating of the internal waves by the two-dimensional models [2,10]: At maximum eastward tidal flow, the interface at the sill (seamount peak) is lifted upward, while an internal tide (interfacial depression) east of the sill is present. At slack tide the tide starts to propagate westward toward the sill. After the tide strides the sill, it disintegrates. At maximum westward tidal flow, the interface at the sill is again lifted upward, while an internal tide west of the sill is present. At slack tide the tide starts to propagate eastward toward the sill. As for the evolution of the westward propagating internal tide, this tide passes the sill and disintegrates.

We now study the generation process of internal tides during a tidal period by the variation of interface displacement. In Fig. 3, the interface displacement in the middle sections of the channel along the east-westward and south-northward directions for eight different times separated by 1/8 of the tidal cycle is shown. The arrows indicate the direction and the strength of the tidal flow at the seamount peak. In the left and right panels, the interface displacement in the middle section of the strait along the east-westward direction (in the following, this section is called section A in short, i.e., the section along $y=61$ in Fig. 2b) and along the south-northward direction (i.e., the section along $x=61$ in Fig. 2b) are shown, respectively. The case in the left panel of Fig. 3 is somewhat different from that by the two-dimensional models: in our model, first, it seems that the induced internal tide doesn't stride the seamount peak before it disintegrates, it only stays near the seamount peak; second, there is no indication of the internal solitary waves propagation after the disintegration of the induced internal tide near the seamount peak. The reason for the first difference may be that, in our three-dimensional model, the maximum tidal velocity changes within $0\sim360^\circ$ with time in a period around the seamount peak, thus the induced internal tide doesn't stride the sill; whereas in the two-dimensional (i.e., in the directions of x and z) model, the tidal current reciprocates from east to west outstandingly, thus the induced internal tide strides the sill at slack tide. Therefore, the stride back and forth over the sill of the induced internal tide in the two-dimensional model is somewhat misleading. The reason for the second difference is because our hydrostatic model fails to describe the propagation of nonlinear internal waves after the disintegration of a tidal baroclinic tide correctly. Similar case could be found in the right panel of Fig. 3. The clear scenes of the internal tide disintegration are shown from the interface displacement in section A for eight different times separated by 1/48 of the tidal cycle (i.e., from 8T/48 to 15T/48, Fig. 4). We can notice that the interface displacement in the western channel fluctuates up and down. The bottom of the induced 'V'-like internal tide begins to distort before its disintegration at about 7T/48 (figure omitted). Does the variation of internal tides have a similar period like tidal current? The variation of the interface displacement in section A with time versus distance from the west to east of the channel is also shown in Fig. 5, the small 'spot-like' signals shown as isolated contours at

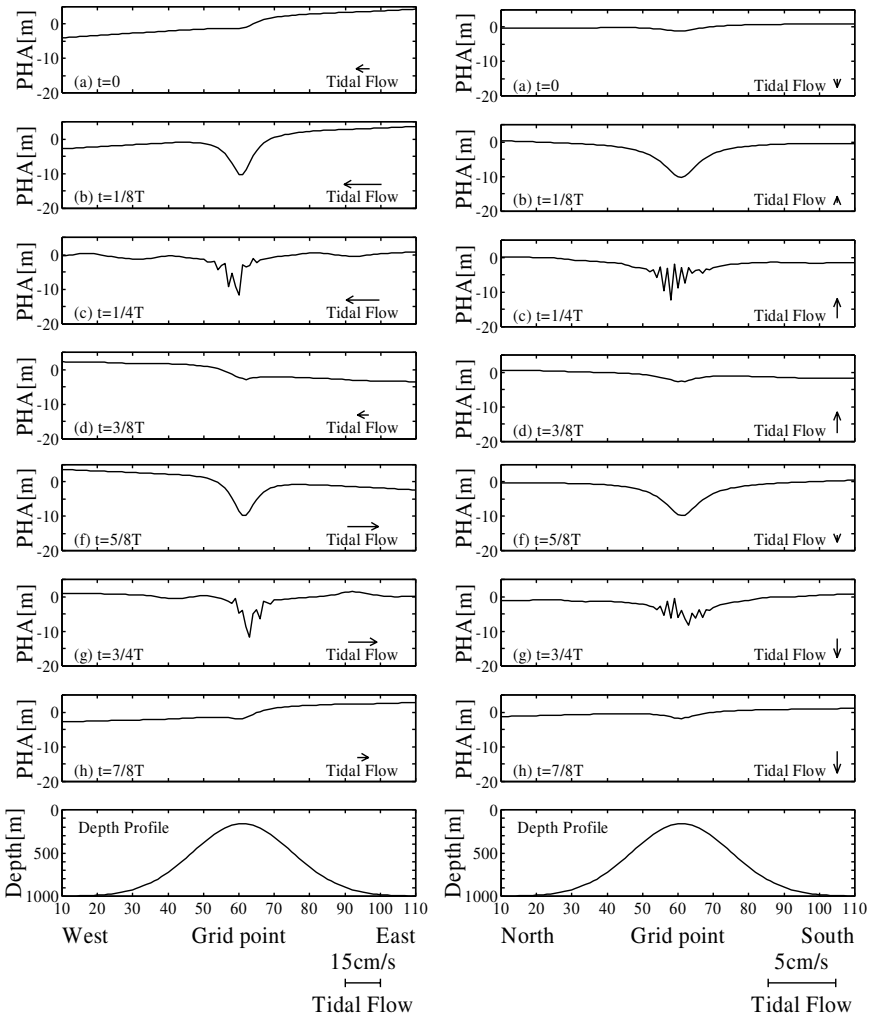

Figure 3: Space-time evolution of the interface displacement (m) for eight different times at the 6th period in experiment E1. The left panel is at section A, along the middle channel in x-direction, and the right panel is along the middle channel in y-direction. This shows the generation of internal tides around the seamount peak.

about 2.2T and 2.7T indicate that the disintegrating of the internal tides happen twice in a tidal period.

Now we have a look at the variation of sea surface and interface displacement fields before and after the disintegration of internal tides. Fig. 6 shows some snap-shots of the sea surface displacement and the interface displacement fields at 7T/48 before the disintegration of the internal tide and at 10T/48 after its disintegration (note that the cross "+" denotes the position of the seamount peak). Before the internal tide disintegrates at 7T/48, there are some alternating bright/dark wave bands (in fact, these bands are the alternating high/low variation gradient of the water elevation) in the sea surface

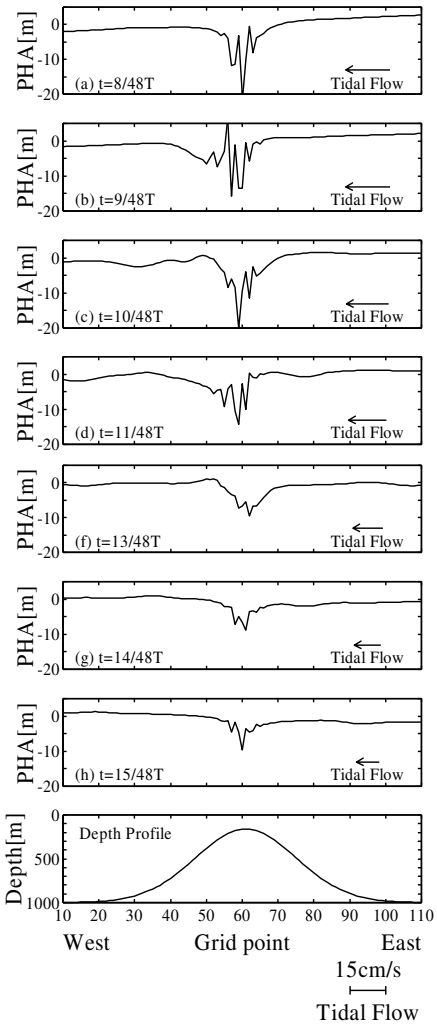

Figure 4: Space-time evolution of the interface displacement (m) in section A for eight different times separated by 1/48 of the tidal cycle in experiment E1. This shows the clear scenes of the internal tide disintegration with time.

displacement and the interface displacement fields (Figs. 6a, c); the internal tide begins to disintegrate at about 8T/48 (Fig. 4), however, there exists no bright/dark wave band in the sea surface displacement field at this time (figure omitted); after the disintegration of the internal tide at 10T/48, the bright/dark wave bands in the sea surface displacement and the interface displacement fields appear again (Figs. 6b, d). This demonstrates that the bright/dark wave bands do not appear continuously during the disintegrating of the internal tide. The horizontal structure of the internal tide is somewhat like a broad bean centered at the seamount peak, the internal tide seems to be trapped by the seamount peak topography. Meanwhile, there exist some separate small bright/dark spots near

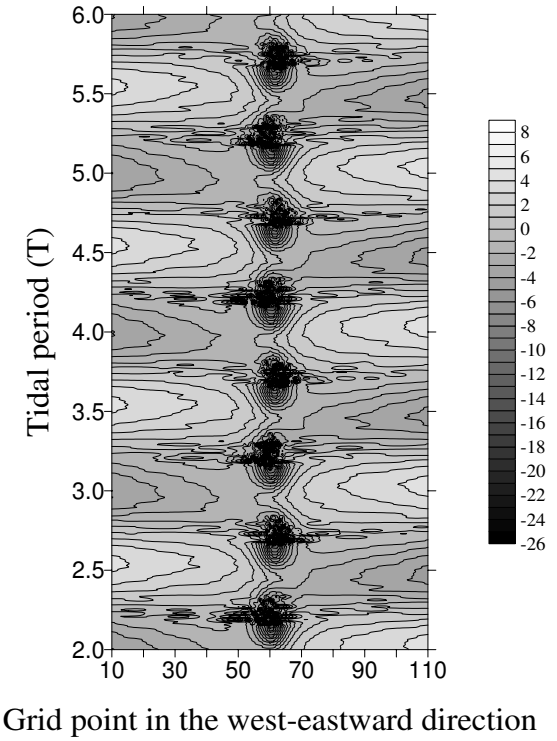

Figure 5: Variation of the interface displacement (m) in section A with time versus distance in experiment E1. This shows the disintegration of internal tides happen twice in a tidal period.

the seamount peak in Fig. 6b and Fig. 6d, which means that the water elevation near the source site of the internal tide changes severely during the disintegration.

It is interesting to discuss the energy densities of both the barotropic and baroclinic tides near the seamount. The barotropic and internal tide energies, averaged over a wave period, are given as [12],

$$E_b = \frac{1}{4}\rho\left\{g\eta_1^2 + H(U_b^2 + V_b^2)\right\}, \tag{3.1}$$

$$E_{it} = \frac{1}{4}\left\{\rho_1[g'\eta_2^2 + h_1(u_{c1}^2 + v_{c1}^2)] + \rho_2 h_2(u_{c2}^2 + v_{c2}^2)\right\}, \tag{3.2}$$

where U_b and V_b are the east and north components of the barotropic tidal flow, u_{c1}, u_{c2}, v_{c1} and v_{c2} are the east and north components of the baroclinic tidal velocity in the upper and lower layers, respectively.

We try to understand the variation of barotropic and baroclinic tidal energies during and after the disintegration of internal tides. Fig. 7 shows the barotropic and baroclinic tidal energies at 8T/48 (during the disintegrating of the internal tide) and 16T/48 (after the disintegration of the internal tide) in experiment E1, respectively. The maximum

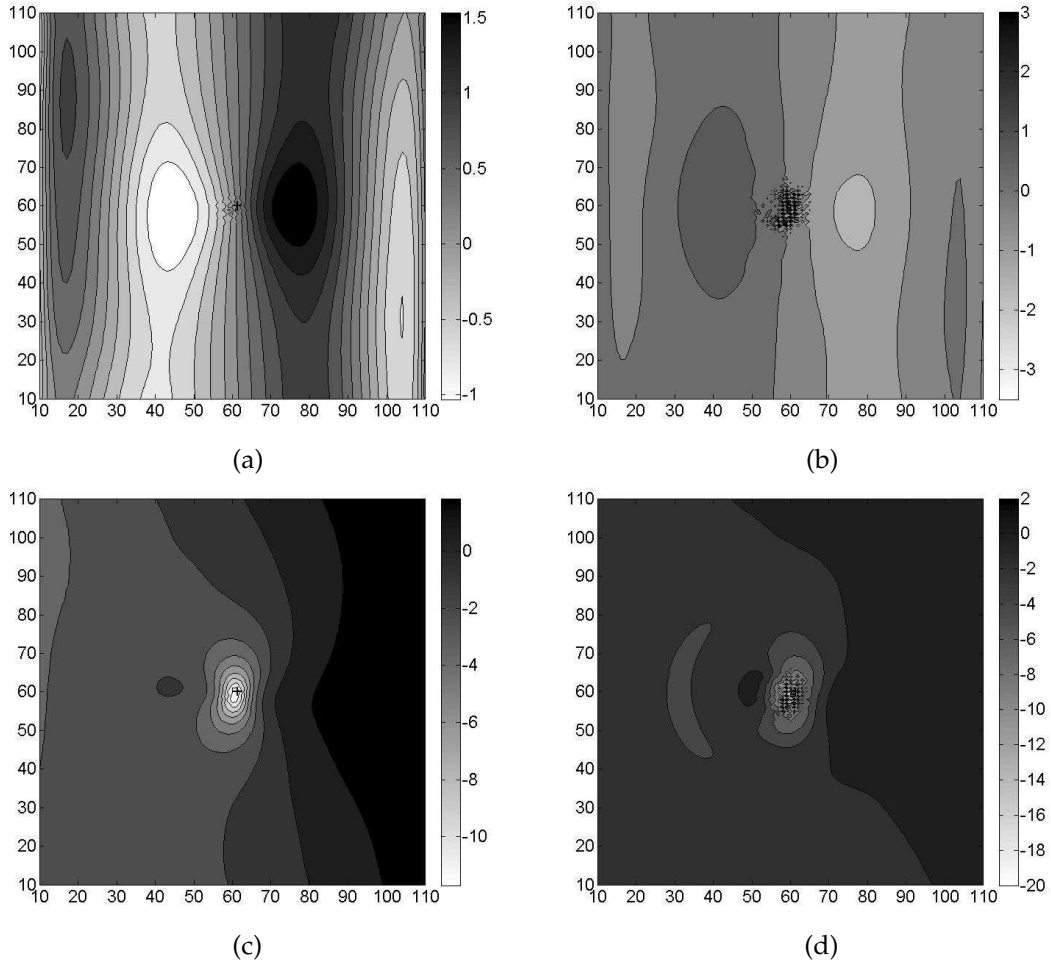

Figure 6: Some snap-shots of the sea surface displacement and the interface displacement fields at 7T/48 before the disintegration of an internal tide and at 10T/48 after its disintegration in experiment E1 (note that the cross "+" denotes the position of the seamount peak). (a) sea surface displacement (cm) at 7T/48, (b) sea surface displacement (cm) at 10T/48, (c) interface displacement (m) at 7T/48, and (d) interface displacement (m) at 10T/48. This shows the variation of sea surface and interface displacement fields before and after the disintegration of internal tides.

barotropic tidal energy mainly appears to the south of the seamount peak (i.e., the maximum is centered at near ($x=65$, $y=25$) in Figs. 7a and 7b) other than around the peak, whilst the maximum baroclinic tidal energy appears around the peak (i.e., the maximum is centered at near (x=61, y=61) in Figs. 7c and 7d). Usually, the barotropic tidal energy is larger than the baroclinic one for the whole domain (e.g., Figs. 7b and 7d), however, during the disintegrating of the internal tide, the baroclinic tidal energy around the seamount peak is much larger than the barotropic one (Figs. 7a and 7c). Moreover, the baroclinic tidal energy seems to reduce rapidly and radiate away from the seamount peak, which

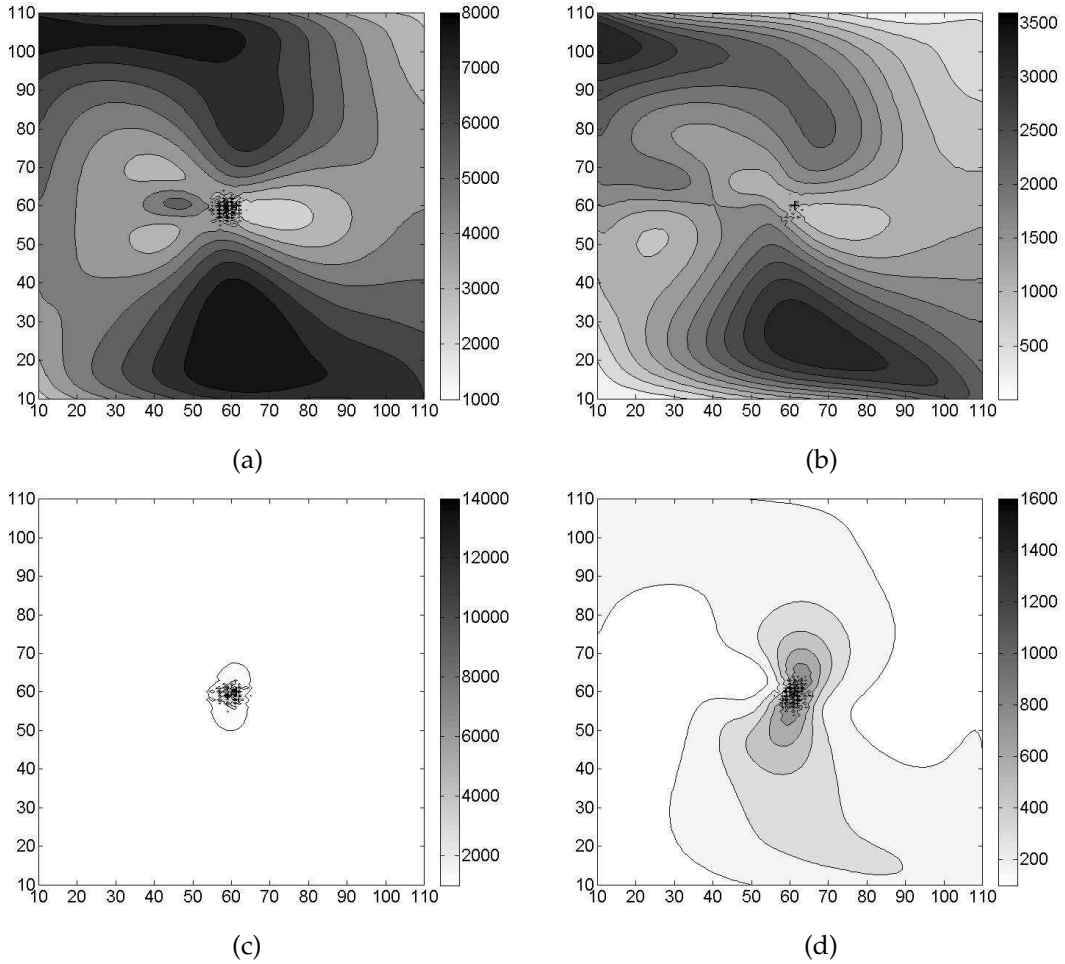

Figure 7: Distribution of the (a) barotropic tidal energy (unit: W/m, here and subsequently) at 8T/48, (b) barotropic tidal energy at 16T/48, (c) baroclinic tidal energy at 8T/48, and (d) baroclinic tidal energy at 16T/48 in experiment E1. This shows the variation of barotropic and baroclinic tidal energies during and after the disintegration of internal tides.

agrees with a linearised three-dimensional model results (Baines, 2007), although the seamount shapes in both studies are different.

3.2 Experiments E2-E8

In the following, another 7 experiments (Table 1) are carried out. Here we choose the result in experiment E1 as the comparison standard. In experiment E2, the former symmetric seamount is elongated into a ridge whose broad axis is oriented along the channel; in experiment E3, the former steep slope with an angle up to 27.8° is reduced to that with an angle of 12.1°; in experiments E4-E5, the initial upper layer depths are shallowed and

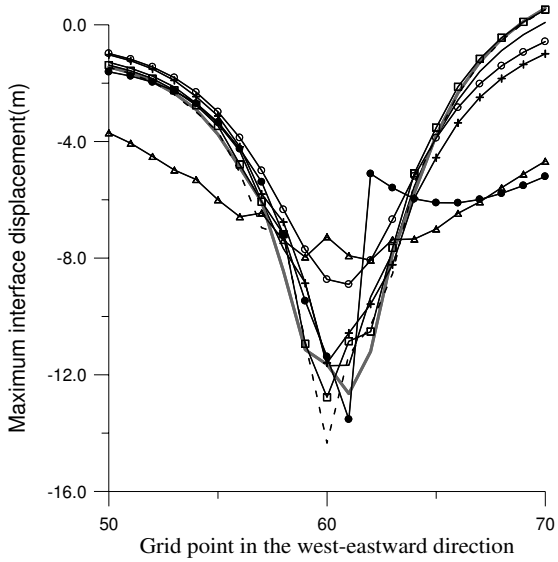

Figure 8: Comparison of the maximum amplitudes of the internal tides in part of section A in the eight experiments (note: E1-solid line, E2- thick grey line, E3-triangular line, E4-circled line, E5-squared line, E6-dashed line, E7- crossed line and E8- blocked circled line). This shows that the disintegration of the internal tide is associated with the amplitude of internal tides.

deepened, respectively; in experiment E6, the imposing tidal flow amplitude at east open boundary is enlarged; in experiment E7, a constant westward background current is exerted; and in experiment E8, the slope of the seamount is no longer symmetric, with about 27.8° and 12.1° in the western and eastern half parts of the channel, respectively.

According to the above experimental results, it is found that the disintegration of the internal tide is associated with the amplitude of internal tides. Since the maximum amplitudes of the internal tides may appear at different time, thus, comparison of the maximum amplitudes of the internal tides in part of section A in the former half of the tidal period (i.e., before the disintegration of the internal tide in experiment E1) in the eight experiments is shown in Fig. 8 (here the curves with solid line, thick grey line, triangular line, circled line, squared line, dashed line, crossed line and blocked circled line denote the results of experiments E1, E2, E3, E4, E5, E6, E7 and E8, respectively), the maximum amplitudes of the induced internal tides change largely. According to the simulated results, it is found that, in experiments E2, E5, E6, and E8, the maximum amplitude of the induced internal tide is larger than that in experiment E1, and the induced baroclinic tidal energy are also stronger. The result from experiment E2 agrees with that in [12], they found that, for symmetric seamounts only a weak internal tide is induced; when elongated into a ridge, an energetic internal tide is induced. In experiments E3 and E4, the maximum amplitudes of the induced internal tides are much less than that in experiment E1, thus the internal tides fail to disintegrate, correspondingly, the variation of sea surface and velocity fields in a tidal period are regular and small. However, even no dis-

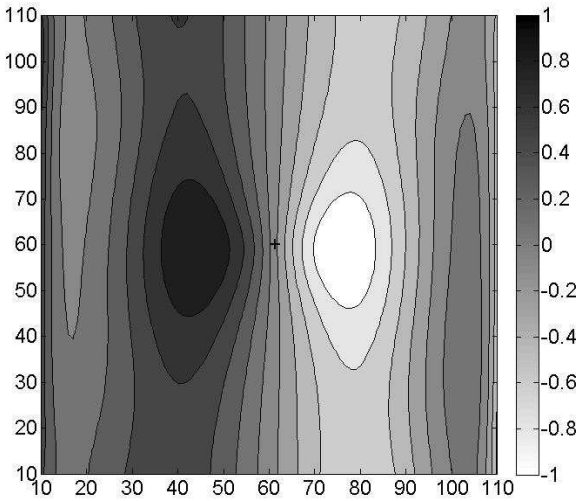

Figure 9: Snap-shot of the sea surface displacement (cm) at 10T/48 in experiment E4. This shows that even there is no disintegration of the internal tide, there also exist some bright/dark wave bands in the sea surface displacement fields.

integration of the internal tide happens, there also exists some bright/dark wave bands in the sea surface displacement fields, e.g., this phenomenon could be shown in the sea surface displacement fields at 7T/48 (figure omitted) and 10T/48 (Fig. 9) in experiment E4, but the variation gradient of the sea surface displacement is much less than that in experiment E1 (Fig. 6b). The major difference between experiments E1 and E4 is that, the current velocity and the water elevation fields in experiment E1 change severely during the disintegrating of the internal tide, whilst those in experiment E4 change smoothly since there is no internal tide disintegration in this case, e.g., Fig. 10 (here the curves with solid line and dashed line denote the results of experiments E1 and E4, respectively) shows the comparison of the time series of the mean upper layer current velocities at the same position (x=60, y=61) near the seamount peak in the these two experiments. Thus, it is not enough to distinguish whether there exist internal solitary waves in some sea areas or not only based on the SAR images [26–28], sometimes the in situ observational hydrologic data (such as the data of current speed, temperature and water elevation, etc.) are needed to support the conclusion. In fact, we can notice that there exist some separate small bright/dark spots near the source site of the internal waves in Fig. 6b other than in Fig. 9, which means that the water elevation near the source site changes severely during the disintegrating of the internal tide.

In experiments E7 and E8, the disintegration of the internal tide happens only one time in a tidal period. In experiment E7, only when both the maximum tidal flow and the background current are westward does the induced internal tide disintegrates, otherwise there is no internal tide disintegration. Fig. 11a shows the comparison of the maximum amplitudes of the internal tides in part of section A at an interval of T/2 (here

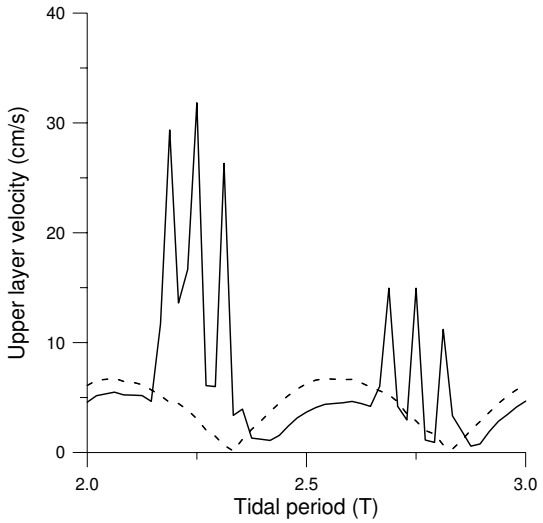

Figure 10: Comparison of the time series of the mean upper layer current velocities (cm/s) at the grid point ($x=60$, $y=61$) near the seamount peak in experiments E1 and E4 (note: E1-solid line, E4-dashed line). This shows the difference of the variation of the current fields for the cases with and without a disintegration of the internal tide.

the curves with solid line and dashed line denote the results at 10T/48 and 34T/48, respectively) in experiment E7. The maximum internal tide amplitude at 10T/48 (i.e., just before the disintegration of the internal tide) is about 7m larger than that at 34T/48 (then no disintegration of the internal tide happens afterwards). This demonstrates that, in the presence of a constant mean background current, when the imposing tidal flow is against the background current, then the background current has a great damping effect on the induced internal tide. This conclusion agrees with the previous two-dimensional composite model results [2]. Fig. 11b also shows the comparison of the maximum amplitudes of the internal tides in part of section A at an interval of T/2 (here the curves with solid line and dashed line denote the results at 10T/48 and 34T/48, respectively) in experiment E8. It is found that, only in the western part of the channel where the slope of the mount is steep does the induced internal tide is large enough to disintegrate, whereas in the eastern part of the channel where the slope of the seamount is gentle, there is no internal tide disintegration.

It is also found that, whether an induced internal tide disintegrates or not is associated with the Froude number. Here, if the composite Froude number F, defined by

$$F^2=\frac{v_1^2}{g\prime h_1}+\frac{v_2^2}{g\prime h_2} \tag{3.3}$$

is larger than 1, the flow is supercritical. Meanwhile, a Richardson number is defined by

$$R_i=-\frac{g}{\rho}\frac{\partial\rho}{\partial z}/\left[(\frac{\partial u}{\partial z})^2+(\frac{\partial v}{\partial z})^2\right]\approx\frac{0.5g'(h_1+h_2)}{[(u_1-u_2)^2+(v_1-v_2)^2]}, \tag{3.4}$$

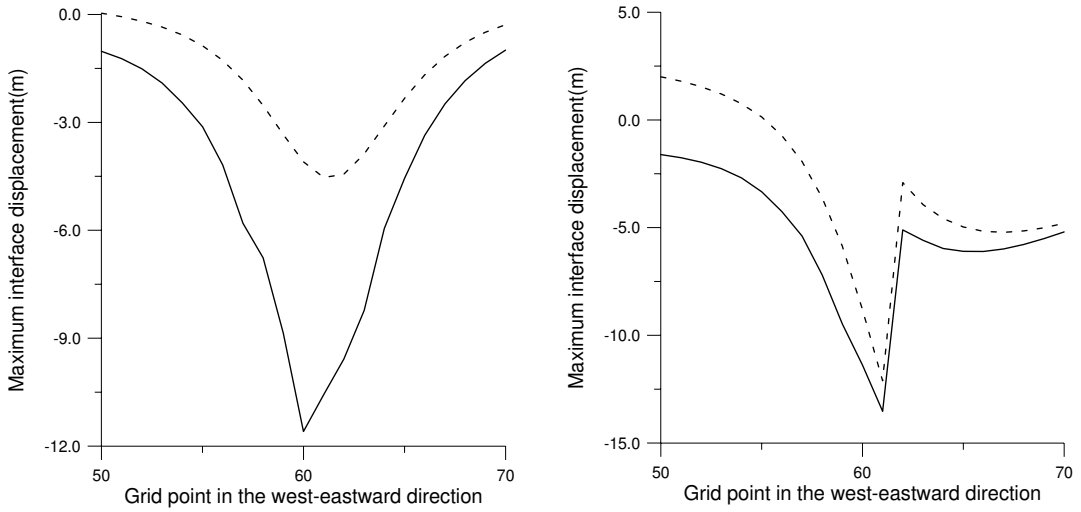

Figure 11: Comparison of the maximum amplitudes of the internal tides in part of section A at an interval of T/2 (at 10T/48-solid line, at 34T/48-dashed line) (a) in experiment E7 and (b) in experiment E8. This shows the effects of the background current and the slope of the seamount on the disintegration of the internal tide.

where u_1, u_2, v_1 and v_2 are the east and north components of the depth-mean tidal velocity in the upper and lower layers, respectively. Fig. 12 shows the comparison of the variations of maximum Froude number and minimum Richardson number for the whole field in a tidal period in the eight experiments (here the curves with solid line, thick grey line, triangular line, circled line, squared line, dashed line, crossed line and blocked circled line denote the results of experiments E1, E2, E3, E4, E5, E6, E7 and E8, respectively). The maximum Froude number and minimum Richardson number always appear near the seamount peak. In the above experiments, only the maximum Froude number in experiments E3 and E4 is always less than 1, thus the corresponding amplitude of the induced internal tide is too small to disintegrate (Fig. 12a). In the other experiments, once when the maximum Froude number approaches 1 during a tidal period, the bottom of the induced 'V'-like internal tide would distort, and then after the maximum Froude number gets larger than 1, the distorted internal tide begins to disintegrate. In experiments E1, E2, E5 and E6, the disintegration of an internal tide happens twice in a tidal period, corresponding to the maximum Froude number larger than 1 at about $t = 2.16$T and t=2.68T, whilst in experiments E7 and E8, it happens only one time in a period, corresponding to the maximum Froude number larger than 1 at about t=2.25T in experiments E7 and about $t = 2.71$T in experiments E8, respectively. In all of the experiments except experiment E2, the minimum Richardson number is always greater than 1/4 (note that in Fig. 12b, the y-axis is labeled in $\log_{10}$ form and every mark value increases 0.1 when the Richardson number is less than 1), which agrees with the sufficiency criterion $R_i > 1/4$ for stability of shear flow of a stratified fluid [29]. However, in experiment E2, at about

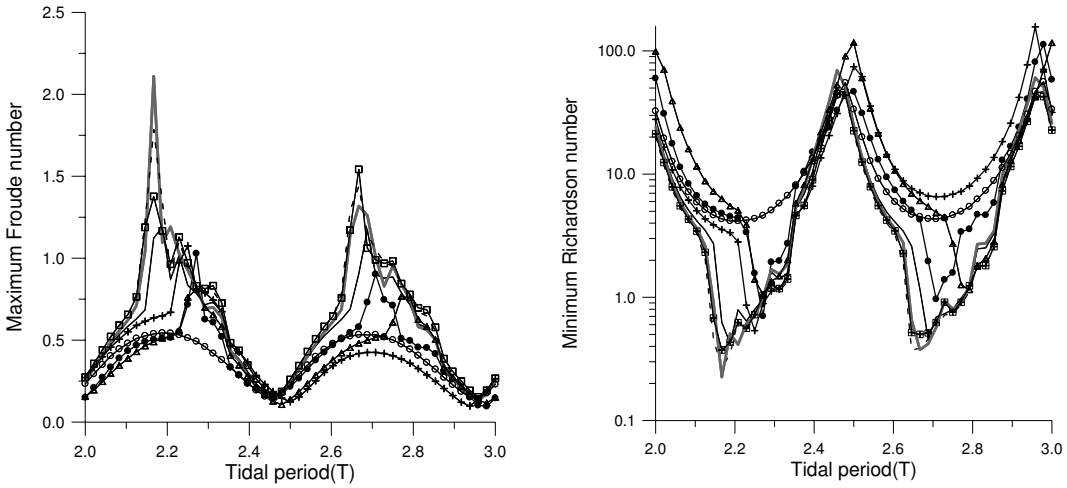

Figure 12: Comparison of the variations of maximum Froude number and Richardson number in a tidal period. (a) Froude number, and (b) Richardson number (note: E1-solid line, E2- thick grey line, E3-triangular line, E4-circled line, E5-squared line, E6-dashed line, E7- crossed line and E8- blocked circled line. In Fig. 12b, the y-axis is labeled in $\log_{10}$ form and every mark value increases 0.1 when the Richardson number is less than 1). This shows that the maximum Froude number and the minimum Richardson number vary with different experimental conditions.

$t = 2.17$T, the minimum Richardson number reaches 0.225, the current field is still stable, this may be due to the error caused by the two-layer stratified fluid model itself, but in our additional experiment, if the imposing tidal flow is strengthened based on experiment E2, the minimum Richardson number would get even smaller, the corresponding current field gets unstable and the model running is divergent thereafter.

According to the above experiments, it is shown that, whether an induced internal tide disintegrates or not depends on the Froude number. Once when the Froude number is larger than 1, the associated maximum amplitude of the induced internal tide is so large that the internal tide could disintegrate, whilst when the Froude number is less than 1, the associated maximum amplitude of the induced internal tide is too small to disintegrate. This can also be clearly shown by the comparison of the variations of Froude number versus the amplitude of the internal tide with time for only 1/4 of a tidal period in experiments E1 and E3 (Fig. 13). In experiment E1, the internal tide could disintegrate after the Froude number gets larger than 1, whilst in experiment E3, no disintegration of internal tide happens since the Froude number is always less than 1.

Whether the Froude number can reach 1 or not, it depends on the seamount feature, the slope, the initial upper layer depth and the imposing driven force including the tidal flow and the background current. According to Eq. (3.3) and the additional experiment based on experiment E2, for the specific stratification, the tidal flow velocity seems to be the most important and sensitive factor affecting the Froude number. Generally speaking,

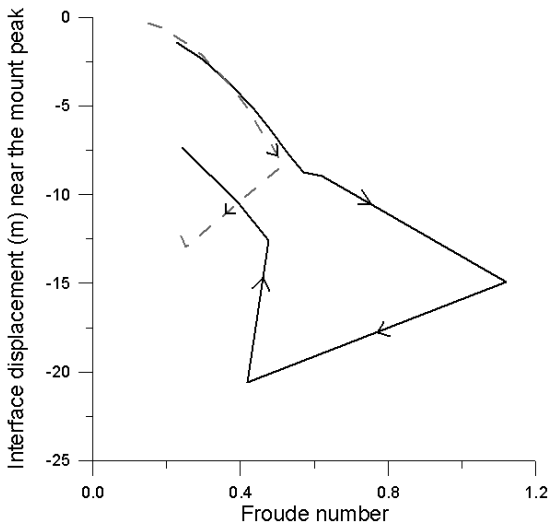

Figure 13: Comparison of the variations of Froude number versus the amplitude of the internal tide with time for only 1/4 of a tidal period at the grid point ($x=59$, $y=61$) near the seamount peak in experiments E1 and E3 (note: E1-solid line, E3- dashed line, the variation of the variables with time is along the arrow direction). This shows the condition for the disintegration of the internal tide.

the Richardson number $>1/4$ is a criterion for stability of shear flow of a stratified fluid.

In the Luzon Strait, since the background current in the Luzon Strait is not always westward [5,6], thus the uni-directional (only westward) propagation of the internal solitary waves may be due to the asymmetrical slope of the sill channel in the Luzon Strait, in fact, in the channel between the Batan and Sabtang islands, the sill slope facing the SCS is steeper than that facing the Pacific [1].

4 Conclusion

In this paper, a three-dimensional two-layer model is employed to study the generation of internal tides by tidal flows over a submerged seamount in the channel. Several numerical experiments with different topographic features, upper layer depths, tidal flows and background currents are carried out to study the variations of the internal tide generations. According to the above experimental results, the following conclusions can be reached:

For the specific stratification, the seamount feature, the slope, the initial upper layer depth and the imposing tidal flow and background current determine the Froude number near the seamount peak. When the Froude number is less than 1, the induced barotropic tidal energy is larger than the baroclinic one, and the maximum barotropic tidal energy mainly appears to the south of the seamount peak, whilst the maximum baroclinic tidal energy appears around the peak, where it reduces rapidly and radiates away from the

peak. When the Froude number is larger than 1, the associated maximum amplitude of the induced internal tide is so large that the bottom of its shape begins to distort, finally it disintegrates; meanwhile, the current velocity and the water elevation fields change severely during the disintegrating of the internal tide, and the baroclinic tidal energy around the seamount peak is much larger than the barotropic one. The Richardson number $>1/4$ is a criterion for stability of shear flow of a stratified fluid.

Since in the three-dimensional model, the maximum tidal velocity changes within $0\sim360^\circ$ with time around the sill, the induced internal tide does not stride the sill before it disintegrates, which is different from the two-dimensional model results.

The possible reason for the uni-directional propagation of the internal solitary waves in the northern SCS may be related to the asymmetrical slope of the sill channel in the Luzon Strait.

Acknowledgments

Authors are indebted to Prof. R. N. Ibragimov and an anonymous referee for helpful comments. This work is jointly supported by the Key Program KZCX1-YW-12-03 from the Chinese Academy of Sciences, "863" Hi-Tech Programs (Nos. 2008AA09Z112 and 2008AA09A402), NSFC Grant No. 40676021 and National Special Project 2006BAB19B01, and Grant 2007B030200004 from Guangdong Province of China.

References

[1] C. C. Ebbesmeyer, C. A. Coomes, R. C. Hamilton, K.A. Kurrus, T.C. Sullivan, B.L. Salem, R.D. Romea and R.J. Bauer, New observation on internal wave(solitons) in the South China Sea using an acoustic doppler current profiler, Marine Technology Society 91 Proceedings, New Orleans, 1991, 165-175.

[2] S. Cai, X. Long and Z. Gan, A numerical study of the generation and propagation of internal solitary waves in the Luzon Strait, Oceanol. Acta, 25(2) (2002), 51-60.

[3] M. K. Hsu and A. K. Liu, Nonlinear internal waves in the South China Sea. Canadian Journal of Remote Sensing, 26(2000), 72-81.

[4] Q. Zheng, R. D. Susanto, C. R. Ho, Y.T. Song and Q. Xu, Statistical and dynamical analyses of generation mechanisms of solitary internal waves in the northern South China Sea, J. Geophys. Res, 112 (C3) (2007), C03021.

[5] J. Xu, M. Shi, B. Zhu and Z. Liu, Several characteristics of water exchange in the Luzon Strait, Acta Oceanol. Sinica, 23(1) (2004), 11-21.

[6] Y. Yuan, G. Liao and C. Yang, The Kuroshio near the Luzon Strait and circulation in the northern South China Sea during August and September 1994, J. Oceanogr., 64(5) (2008), 777-788.

[7] T. Hibiya, Generation mechanism of internal waves by a vertically sheared tidal flow over a sill, J. Geophys. Res., 95(1990), 1757-1764.

[8] A. Longo, M. Manzo and S. Pierini, A model for the generation of nonlinear internal tides in the Strait of Gibraltar. Oceanol. Acta, 15(1992), 233-243.

[9] S. Pierini, A model for the Alboran Sea internal solitary waves, J. Phys. Oceanogr., 19(1989), 755-772
[10] P. Brandt, A. Rubino, W. Alpers and J.O. Backhaus, Internal waves in the Strait of Messina studied by a numerical model and synthetic aperture radar images from the ERS 1/2 satellites, J. Phys. Oceanogr., 27(1997), 648-663.
[11] B.D. Dushaw, B.D. Cornuelle, P.F. Worcester, B.M. Howe and D.S. Luther, Barotropic and baroclinic tides in the central North Pacific Ocean determined from long range reciprocal acoustic transmissions, J. Phys. Oceanogr., 25(1995), 631-647.
[12] P.E. Holloway and M.A. Merrifield, Internal tide generation by seamounts, ridges, and islands, J. Geophys. Res, 104(C11) (1999), 25937-25951.
[13] A. Beckmann and D.B. Haidvogel, A numerical simulation of flow at Fieberling Guyot, J. Geophys. Res, 102(C31) (1997), 5595-5613.
[14] D.R. Goldner and D. Chapman, Flow and particle motion induced above a tall seamount by steady and tidal background currents, Deep Sea Res. I, 44(1997), 719-744.
[15] P. G. Baines, Internal tide generation by seamounts, Deep?Sea Res. I, 54(2007), 1486-1508.
[16] C. Garrett and E. Kunze. Internal tide generation in the deep ocean. Ann. Rev. Fluid Mech., 39(2007), 57-87.
[17] R. N. Ibragimov, Generation of internal tides by an oscillating background flow along a corrugated slope, Phys. Scr. 78(2008), 065801.
[18] R. N. Ibragimov and D. E. Pelinovsky, Three-dimensional gravity waves in a channel of variable depth, Communications in Nonlinear Science and Numerical Simulation, 13(2008), 2104-2113.
[19] A. E. Gill, Atmosphere-Ocean Dynamics, Academic Press, New York, 1982, 119-127.
[20] H. E. Hurlburt and J. D. Thompson, A numerical study of Loop Current instrusions and eddy shedding in Gulf of Mexico. J. Phys. Oceanogr., 10(1980), 1611-1631.
[21] S. Cai and W. Wang, A numerical study on the circulation mechanism in the northeastern South China Sea and Taiwan Strait, Tropic Oceanology, 16(1)(1997), 7-15 (in Chinese with English abstract).
[22] I. Orlanski, A simple boundary condition for unbounded hyperbolic flows, J. Comput. Phys., 21(1976), 251-269.
[23] J.A. Lorenzzetti and N. L. Thomas, Two-layer model of summer circulation on the southeast U.S. continental shelf, J. Phys. Oceanogr., 18(1988), 591-608.
[24] A. Grammeltvedt, A survey of finite-difference schemes for the primitive equations for a barotropic fluid. Mon. Wea. Rev., 97(1969), 384-404.
[25] W. R. Holland and L. B. Lin, On the generation of mesoscale eddies and their contribution to the oceanic general circulation I. A preliminary numerical experiment, J. Phys. Oceanogr., 5(1975), 642-657.
[26] R.F. Gasparovic, J.R. Apel and E.S. Kasischke, An overview of the SAR internal wave signature experiment, J. Geophys. Res, 93(1988), 12304-12316.
[27] J.C.B. da Silva, S.A. Ermakov, I.S. Robinson, D.R.G. Jeans and S.V. Kijashko, Role of surface films in ERS SAR signatures of internal waves on the shelf 1. Short-period internal waves, J. Geophys. Res., 103(C4)(1998), 8009-8031.
[28] Q. Zheng, Y. Yuan, V. Klemas and X. Yan, Theoretical expression for an ocean internal soliton synthetic aperture radar image and determination of the soliton characteristic half width, J. Geophys. Res., 106(C12) (2001), 31415-31423.
[29] J.W. Miles, On the stability of heterogeneous shear flows, J. Fluid Mech., 10(1961), 496-508.